Sensorless Control of Permanent Magnet Synchronous Motor Based on Tracking Differentiator-Frequency-Locked Loop

Sibo WAN, Huimin WANG, Yun ZUO, Gaoli GUO, and Xinglai GE

***Abstract*—Sensorless control technique is regarded as the enabler of the reliability improvements for interior permanent magnet synchronous motor (IPMSM) drives. However, the conventional estimation schemes by using the phase-locked loop (PLL) and the frequency-locked loop (FLL) may experience undesired accuracy under acceleration and deceleration cases (ADCs). To address this, a speed estimation scheme by combining a closed-loop active flux observer (CLAFO) with a tracking differentiator-based frequency-locked loop (TD-FLL) was proposed in this paper. Starting from a brief introduction of the conventional PLL performance analysis with - and FLLADCs based estimation schemes, a detailed is provided. Accordingly, an estimation scheme based on the TD-FLL is elaborated. Considering the performance of the proposed TD-FLL scheme is adversely affected by various disturbances, a CLAFO is carefully designed to improve the disturbance immunity of the proposed TD-FLL scheme. Extensive experimental tests are conducted to verify the effectiveness of the proposed TD-FLL scheme under different test cases.**

***Index Terms*—Closed-loop active flux observer (CLAFO), frequency-locked loop (FLL), interior permanent magnet synchronous motor (IPMSM), sensorless control, tracking differentiator (TD).**

I. Introduction

INTERIOR permanent magnet synchronous motor (IPMSM) is widely used in industrial production and traction transmission due to its advantages of high power density, high operating efficiency and large starting torque [1]–[4]. In most high performance IPMSM drive systems, precise speed sensors are needed to realize the feedback of speed information. However, the use of speed sensors will increase the cost of the system and reduce the reliability of the system. Due to the different operating environment of the motor, such as in the harsh conditions of high temperature and high humidity vibration, the speed sensor becomes one of the main fault sources of the motor. When the fault of the speed sensor occurs, it will seriously affect the control performance of the motor. Thus, to improve the reliability of motor operation, there is a growing trend to implement sensorless control through various speed estimation schemes to replace speed sensors [5], [6].

The model-based method is based on the mathematical. model of IPMSM, which is mainly used in medium- and highspeed range [7]–[14]. The model-based method attract much popularity in sensorless motor control include sliding mode observer (SMO) for observing the extended back electromotive force (EMF) [7], [8], flux observer method for observing active flux [9], [10], the model reference adaptive system (MRAS) [11], [12], extended Kalman filter (EKF) [13] and extended state observer (ESO) [14], etc. The SMO used to observe the extended back EMF has the characteristics of simple structure and high robustness, but the signal-to-noise ratio is low and there is oscillation in the low-speed domain. The flux observer method decouples the observation signal from the speed information, it has a better low-speed performance. The observed flux method is more efficient and accurate than the observed back EMF method to obtain the speed and position information. Therefore, a closed-loop active flux observer (CLAFO) for IPMSM is established to obtain active information in this paper.

Phase-locked loop (PLL) and frequency-locked loop (FLL) are of great significance in the field of power and energy applications, both technologies have been applied extensively in the sensorless control for IPMSM drives attributable to high simplicity and flexibility. However, most of the sensorless control strategies based on PLL and FLL show poor control performance when the motor runs frequently in the accelerate and decelerate conditions, such as subway and new energy vehicles. Therefore, in view of the inevitable estimation error of conventional PLL and FLL under acceleration and deceleration cases (ADCs), many studies have been done to improve the estimation performance by optimizing the structure of the PLL and FLL. The conventional PLL can be regarded as a type-2 control system based on proportional-integral (PI) controller

Manuscript received September 24, 2024; revised October 14, 2024; accepted October 31, 2024. Date of publication December 30, 2024; date of current version November 21, 2024. This work was supported in part by National Natural Science Foundation of China under Grant 52307068 and in part by National Natural Science Foundation of Sichuan Province under Grant 2023NSFSC0824. *(Corresponding author: Huimin Wang.)*

S. Wan and G. Guo are with the Ministry of Education Key Laboratory of Magnetic Suspension Technology and Maglev Vehicle, Southwest Jiaotong University, Tangshan Institute, Chengdu 610031, China (e-mail: 2023210836@my.swjtu.edu.cn; 13298180356 @swjtu.edu.cn).

H. Wang, Y. Zuo, and X. Ge are with the Ministry of Education Key Laboratory of Magnetic Suspension Technology and Maglev Vehicle, Southwest Jiaotong University, Chengdu 610031, China (e-mail: wanghuimin@my.swjtu.edu.cn; z_uoy_un@my.swjtu.edu.cn; xlge@swjtu.edu.cn).

Digital Object Identifier 10.24295/CPSSTPEA.2024.00025

loop filter, and the phase steady-state error cannot be guaranteed to be eliminated under ADCs. A desirable way is to eliminate the steady-state error by increasing the type order of the PLL system [15]–[17]. [15] and [16] presented the existence of two poles in a loop filter of the type-3 PLL scheme, which improved estimation performance under ADCs. The dual-loop synchronous reference frame-PLL scheme for sensorless drive system was proposed to achieve satisfactory speed estimation performance under ADCs in [17]. However, increasing the order of PLL will cause the deterioration of system stability margin and dynamic performance. In addition, a unit delay compensation scheme for type-2 PLL was introduced to eliminate the steady state error during the frequency ramp in [18], but it increases the complexity of parameter adjustment and structure. Applying second-order generalized integrator frequency-locked loop (SOGI-FLL) and reduced-order generalized integrator frequency-locked loop (ROGI-FLL) schemes for speed estimation are typical examples of FLL. Adaptive SOGI-FLL and adaptive ROGI-FLL schemes were introduced in [19], combines the super-twisting algorithm (STA) with a new structure of FLL scheme was proposed in [20]. [19] and [20] can achieve error-free tracking under ADCs, but the requirement for speed information feedback has a negative impact on the dynamic performance of the system. A novel type-1 FLL scheme with selective pre-filter in the front stage and out-loop compensation to obtain the same features of type-2 FLL in response to frequency drift was explored in [21]. Similarly, the compensation scheme increases the complexity of the system.

In this paper, a speed estimation scheme based on tracking differentiator-FLL (TD-FLL) is proposed to achieve satisfactory estimation performance under ADCs. Meanwhile, the active flux is be accurate estimated by using the CLAFO even with DC offset and part motor parameter variations during practical IPMSM drives operation.

The rest of this paper is organized as follows. In Section II, the implementation of conventional PLL and FLL is introduced, and the mechanism of estimating performance deterioration under ADCs is analyzed in detail. In Section III, presents the details of the TD-FLL scheme, and points out the advantage of speed estimation under ADCs. Then, Section IV presents the implementation process of the CLAFO with considerable robustness. The anti-interference performance of the CLAFO with DC offset and part motor parameter mismatch is analyzed in detail is conducted in Section V. Experimental validation is given in Section VI. Finally, Section VII concludes this article.

II. Performance Analysis of Conventional PLL and FLL Schemes Under ADCs

A. Performance Analysis of the Conventional PLL Scheme

A typical quadrature phase-locked loop (QPLL) scheme applied in IPMSM drives is shown in Fig. 1, in which ψ_α and ψ_β are the flux with position information. The QPLL scheme is mainly composed of three parts: phase detector (PD), loop filter (LF) and voltage-controlled oscillator (VCO). With Fig. 1, the small-signal model of the QPLL scheme is shown in Fig. 2.

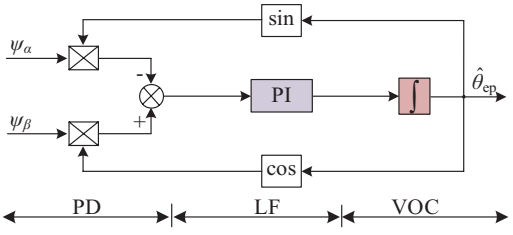

Fig. 1. Block diagram of the conventional QPLL scheme.

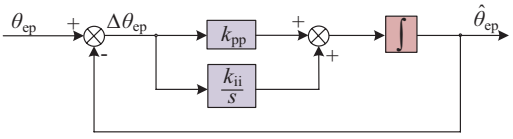

Fig. 2. Small-signal model of the conventional QPLL scheme.

Seen from Fig. 2, the open-loop transfer function of the QPLL can be obtained as

$$G_{ol}^{QPLL}(s)=\frac{\hat{\theta}_{ep}}{\theta_{ep}-\hat{\theta}_{ep}}=\frac{k_{pp}s+k_{ii}}{s^2} \tag{1}$$

in which θ_{ep}, $\hat{\theta}_{ep}$, $\Delta\theta_{ep}$, k_{pp} and k_{ii} are the input position information of the QPLL scheme, the output position estimation information of the QPLL scheme, the position estimation error of the QPLL scheme, the gains of the LP in the QPLL scheme, respectively. Based on (1), it can be further given by

$$G_{error}^{QPLL}(s)=\frac{\Delta\theta_{ep}}{\theta_{ep}}=\frac{1}{1+G_{ol}^{QPLL}(s)}=\frac{s^2}{s^2+k_{pp}s+k_{ii}} \tag{2}$$

The frequency ramp input (h/s^2) can be equivalent to the position acceleration input (h/s^3). Therefore, the position errorwith frequency ramp input can be expressed as

$$\Delta\theta_{ep}(s)=\lim_{s\to 0}s\cdot\frac{h}{s^3}\cdot G_{error}^{QPLL}(s)=\frac{h}{k_{ii}}\neq 0 \tag{3}$$

where h is the gain of frequency change under ADCs. Seen from (3), the QPLL scheme has a steady-state error in position estimation under ADCs. To reduce the position error of the QPLL scheme estimation, k_{ii} in the LP can be set to a large value. A large value of k_{ii} can improve the dynamic performance and position estimation accuracy of the QPLL scheme, but will adversely affect the steady-state performance of the QPLL scheme. The closed-loop transfer function of the QPLL scheme can be obtained as

$$G_{\mathrm{cl}}^{\mathrm{QPLL}}(s)=\frac{G_{\mathrm{ol}}^{\mathrm{QPLL}}(s)}{1+G_{\mathrm{ol}}^{\mathrm{QPLL}}(s)}=\frac{k_{\mathrm{pp}}s+k_{\mathrm{ii}}}{s^2+k_{\mathrm{pp}}s+k_{\mathrm{ii}}} \tag{4}$$

Afterwards, (4) is rewritten as

$$G_{\mathrm{cl}}^{\mathrm{QPLL}}(s)=\frac{k_{\mathrm{pp}}s+k_{\mathrm{ii}}}{s^2+k_{\mathrm{pp}}s+k_{\mathrm{ii}}}=\frac{2\zeta\omega_{\mathrm{n}}s+\omega_{\mathrm{n}}^2}{s^2+2\zeta\omega_{\mathrm{n}}s+\omega_{\mathrm{n}}^2} \tag{5}$$

where ζ and ω_{n} are the damping factor and the natural frequency, and

$$k_{\mathrm{pp}}=2\zeta\omega_{\mathrm{n}} \qquad k_{\mathrm{ii}}=\omega_{\mathrm{n}}^2 \tag{6}$$

According to (5), the amplitude response of the closed-loop transfer function can be described as

$$\left|G_{\mathrm{cl}}^{\mathrm{QPLL}}(j\omega)\right|=\left|\frac{\omega_{\mathrm{n}}^2+j2\zeta\omega_{\mathrm{n}}\omega}{(\omega_{\mathrm{n}}^2-\omega^2)+j2\zeta\omega_{\mathrm{n}}\omega}\right| \tag{7}$$

The closed-loop transfer function of QPLL can be equivalent to a second-order low-pass filter, the bandwidth frequency of the QPLL scheme can be calculated as

$$\omega_{\mathrm{b}}=\omega_{\mathrm{n}}\sqrt{(1+2\zeta^2)+\sqrt{(1+2\zeta^2)^2+1}} \tag{8}$$

In addition, according to the definition of the noise bandwidth of the QPLL scheme [22], it can be expressed as

$$B_{\mathrm{n}}=\frac{1+4\zeta^2}{8\zeta}\omega_{\mathrm{n}} \tag{9}$$

From (8) and (9), the bandwidth frequency and the noise bandwidth of the system are related to the natural frequency, when maintaining the same ζ. The increase of noise bandwidth will impair the noise immunity of the system, resulting in the deterioration of the steady-state estimation performance of the system.

B. Performance Analysis of the Conventional FLL Scheme

As a typical FLL scheme of IPMSM drives, the block diagram of the SOGI-FLL speed estimation scheme is shown in Fig. 3, in which the $\hat{\psi}_{\alpha\beta}$, $\hat{q\psi}_{\alpha\beta}$, $\hat{\omega}_{ef}$, $\varepsilon_{\alpha\beta}$, k and Γ are the estimated flux, the quadrature term of the estimated flux, the estimated frequency, the frequency error, and the gains of the SOGI-FLL, respectively. The SOGI-FLL scheme is also mainly composed of three parts: two SOGI-based quadrature-signal generators (SOGI-QSGs), a gain normalization unit and a FLL. Fig. 4 presents the simplified model of the SOGI-FLL scheme.

Seen from Fig. 4, the open-loop transfer function of the SOGI-FLL scheme can be obtained as

$$G_{\mathrm{ol}}^{\mathrm{FLL}}(s)=\frac{\hat{\omega}_{ef}}{\omega_{ef}-\hat{\omega}_{ef}}=\frac{2\Gamma}{s} \tag{10}$$

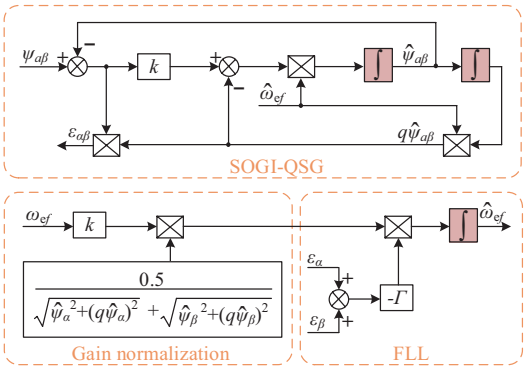

Fig. 3. Block diagram of the SOGI-FLL scheme.

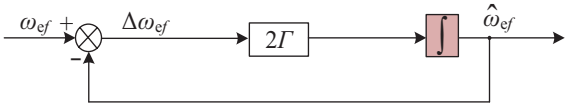

Fig. 4. Simplified model of the SOGI-FLL scheme.

The frequency estimation error transfer function can be calculated as

$$G_{\mathrm{error}}^{\mathrm{FLL}}(s)=\frac{\Delta\omega_{ef}}{\omega_{ef}}=\frac{1}{1+G_{\mathrm{ol}}^{\mathrm{FLL}}(s)}=\frac{s}{s+2\Gamma} \tag{11}$$

When the input frequency is a ramp type, the frequency error can be derived from (11) can be expressed as

$$\Delta\omega_{ef}(s)=\lim_{s\to 0}s\cdot\frac{s}{s+2\Gamma}\frac{h}{s^2}=\frac{h}{2\Gamma}\neq 0 \tag{12}$$

Seen from (12), the SOGI-FLL scheme is unable to achieve error-free tracking under ADCs. A large value of Γ can reduce the steady-state error under ADCs, improve the dynamic performance of the system, but reduce the anti-noise performance of the system. In addition, since the SOGI-FLL scheme requires frequency feedback, this also adversely affects the dynamic performance of the system.

III. Speed Estimation Scheme Based on TD-FLL

Considering the QPLL scheme and the SOGI-FLL scheme fails to provide accurate estimation under ADCs, a simple yet effective estimation scheme based on TD-FLL is developed, which is detailed in this section.

In IPMSM drives, it is clear that

$$\hat{\theta}_{\mathrm{e}}=\arctan\left(\frac{\psi_{\beta}}{\psi_{\alpha}}\right) \tag{13}$$

The estimated speed can be obtained as

$$\hat{\omega}_{\mathrm{e}}=\frac{\mathrm{d}\hat{\theta}_{e}}{\mathrm{d}t}=\frac{\mathrm{d}\left[\arctan\left(\frac{\psi_{\beta}}{\psi_{\alpha}}\right)\right]}{\mathrm{d}t}=\frac{E_{\beta}\psi_{\alpha}-E_{\alpha}\psi_{\beta}}{\psi_{\alpha}^2+\psi_{\beta}^2} \tag{14}$$

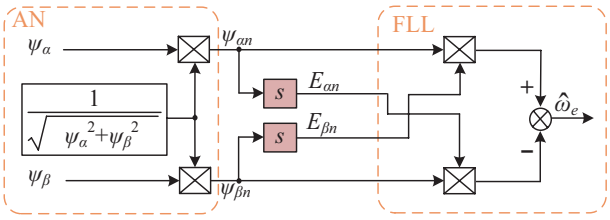

Fig. 5. Block diagram of the CD-FLL scheme.

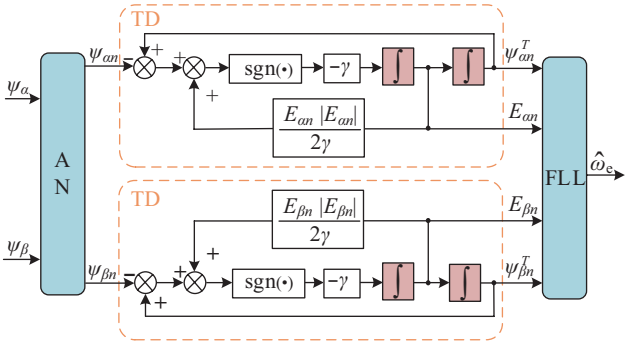

Fig. 6. Block diagram of the TD-FLL scheme.

where $\hat{\omega}_e$, E_α and E_β are the estimated speed, α- and β-axis components of the back EMF, respectively.

After normalizing the amplitude of the flux, (14) can be further expressed as

$$\hat{\omega}_e = \frac{E_\beta \psi_\alpha - E_\alpha \psi_\beta}{\psi_\alpha^2 + \psi_\beta^2} = E_{\beta n}\psi_{\alpha n} - E_{\alpha n}\psi_{\beta n} \tag{15}$$

where $\psi_{\alpha n}$, $\psi_{\beta n}$, $E_{\alpha n}$ and $E_{\beta n}$ are the flux with rotor position information and the back EMF after normalization of flux amplitude. According to (14) and (15) , the speed estimated scheme that includes an amplitude normalization (AN) unit and a conventional differentiator-based FLL (CD-FLL) can be designed as shown in Fig. 5. However, the input of the FLLrequires the differentiation of the flux. The CD-FLL scheme is sensitive to noise and clutter, which may lead to the estimation performance degradation. To mitigate the adverse effects caused by the pure differentiator, the TD is introduced to replace the pure differentiator to obtain the back EMF. The TD is typically expressed as [23]

$$\begin{cases} \dfrac{\mathrm{d}v_1}{\mathrm{d}t} = v_2 \\ \dfrac{\mathrm{d}v_2}{\mathrm{d}t} = -\gamma\,\mathrm{sgn}\left(v_1 - v_r + \dfrac{v_2|v_2|}{2\gamma}\right) \end{cases} \tag{16}$$

where v_1 and v_2 are the state variables, v_r is the reference value of the state variable v_1, and γ is the gain of the TD. Taking the estimated active flux into the TD can be obtained

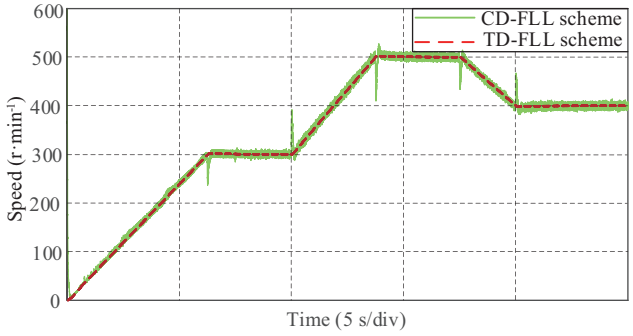

Fig. 7. Estimation performance comparison between the CD-FLL scheme and the TD-FLL scheme.

$$\begin{cases} \dfrac{\mathrm{d}\psi_{\alpha\beta n}}{\mathrm{d}t} = E_{\alpha\beta n} \\ \dfrac{\mathrm{d}E_{\alpha\beta n}}{\mathrm{d}t} = -\gamma\,\mathrm{sgn}\left(\psi^T_{\alpha\beta n} - \psi_{\alpha\beta n} + \dfrac{E_{\alpha\beta n}|E_{\alpha\beta n}|}{2\gamma}\right) \end{cases} \tag{17}$$

in which $\psi^T_{\alpha\beta n}$ is the tracking signal of the $\psi_{\alpha\beta n}$. The block diagram of the TD-FLL scheme can be designed according to (15) and (17), as shown in Fig. 6. The TD-FLL scheme consists of three main parts, i.e., an AN unit of the flux, two TDs and a FLL unit. Speed can be estimated by simple mathematical operations. The TD is used to track the flux signal and obtain the back EMF. Seen from Fig. 7, the TD can avoid the disadvantages of amplifying noise caused by the CD. Therefore, the TD-FLL scheme is expected to achieve error-free tracking under ADCs and ensure excellent dynamic performance and stability margin due to do not introduce the feedback structure and additional parameter variables.

However, the TD-FLL scheme lacks anti-interference ability, and the accuracy of speed estimation depends on the acquisitionof the accurate flux. Taking the presence of DC offset disturbance as an illustrative example, the conventional openloop flux observer model is used to obtain flux information, and the simulation test result is shown in Fig. 8.

IV. Implementation of the CLAFO

A. Introduction of Active Flux

The voltage model (VM) of IPMSM in synchronous reference frame (i.e., *dq* reference frame) can be expressed as

$$\begin{cases} u_d = R_s i_d + L_d \dfrac{\mathrm{d}i_d}{\mathrm{d}t} - \omega_e L_q i_q \\ u_q = R_s i_q + L_q \dfrac{\mathrm{d}i_q}{\mathrm{d}t} + \omega_e L_d i_d + \omega_e \psi_f \end{cases} \tag{18}$$

in which u_d, u_q, i_d, i_q ψ_f, L_d, L_q, R_s and ω_e are d- and q-axis components of the stator voltage, d- and q-axis components of the stator current, the permanent magnet flux, the q- and q-axis

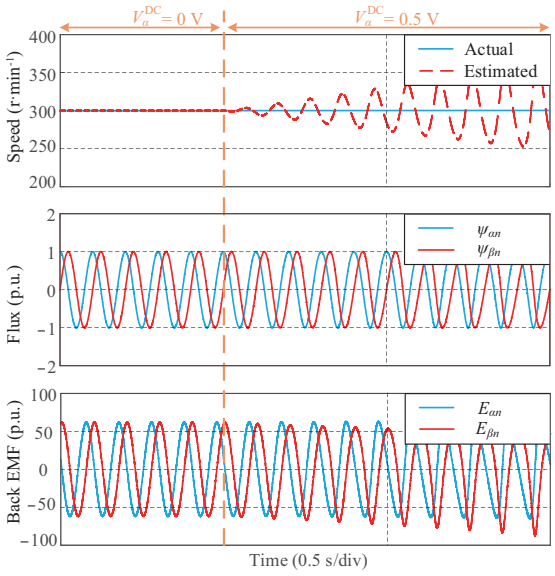

Fig. 8. Estimation performance of the conventional open-loop flux observer model with DC offset.

inductances, the stator resistance and the electrical angular speed. To decouple the position information, (18) can be reexpressed as

$$\begin{cases} u_d = R_s i_d + L_q \dfrac{\mathrm{d}i_d}{\mathrm{d}t} - \omega_e L_q i_q + (L_d - L_q)\dfrac{\mathrm{d}i_d}{\mathrm{d}t} \\ u_q = R_s i_q + L_q \dfrac{\mathrm{d}i_q}{\mathrm{d}t} + \omega_e L_q i_d + \omega_e \psi_f + \omega_e (L_d - L_q) i_d \end{cases} \tag{19}$$

Furthermore, by transforming (19) to the stationary reference frame can be obtained that

$$\begin{cases} u_{s\alpha} = R_s i_{s\alpha} + L_q \dfrac{\mathrm{d}i_{s\alpha}}{\mathrm{d}t} + \dfrac{\mathrm{d}\left[(\psi_f + (L_d - L_q) i_d)\cos\theta_e\right]}{\mathrm{d}t} \\ u_{s\beta} = R_s i_{s\beta} + L_q \dfrac{\mathrm{d}i_{s\beta}}{\mathrm{d}t} + \dfrac{\mathrm{d}\left[(\psi_f + (L_d - L_q) i_d)\sin\theta_e\right]}{\mathrm{d}t} \end{cases} \tag{20}$$

in which $u_{s\alpha}$, $u_{s\beta}$, $i_{s\alpha}$, $i_{s\beta}$ and θ_e are α- and β-axis components of the stator voltage, α- and β-axis components of the stator current, and the rotor position, respectively. The expression of the active flux is defined as

$$\psi_a = \psi_f + (L_d - L_q) i_d \tag{21}$$

The expression of the active flux in the dq reference frame can be expressed as

$$\begin{cases} \psi_{ad} = \psi_f + (L_d - L_q) i_d \\ \psi_{aq} = 0 \end{cases} \tag{22}$$

where ψ_{ad} and ψ_{aq} are d- and q-axis components of the active flux. Obviously, the active flux coincides with the d-axis, and

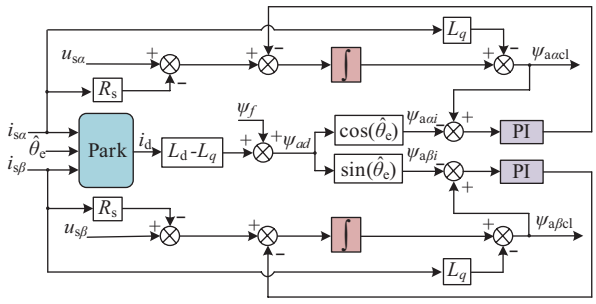

Fig. 9. Block diagram of the CLAFO.

the rotor position information can be decoupled by observing the active flux. From (20) and (22), the expression of the active flux in the stationary reference frame can be expressed as

$$\begin{cases} \psi_{a\alpha v} = \int (u_{s\alpha} - R_s i_{s\alpha})\mathrm{d}t - L_q i_{s\alpha} \\ \psi_{a\beta v} = \int (u_{s\beta} - R_s i_{s\beta})\mathrm{d}t - L_q i_{s\beta} \end{cases} \tag{23}$$

in which $\psi_{a\alpha v}$ and $\psi_{a\beta v}$ are α- and β-axis components of the active flux observed by the VM, respectively.

According to (21) and (22), the active flux in the stationary reference frame can be expressed as

$$\begin{bmatrix} \psi_{a\alpha i} \\ \psi_{a\beta i} \end{bmatrix} = \left[\psi_f + (L_d - L_q) i_d\right] \begin{bmatrix} \cos\hat{\theta}_e \\ \sin\hat{\theta}_e \end{bmatrix} \tag{24}$$

in which $\psi_{a\alpha i}$ and $\psi_{a\beta i}$ are α- and β-axis components of the active flux from the current model (CM).

B. Properties of the CLAFO

The block diagram of the CLAFO is shown in Fig. 9, which the CM and the VM are combined through the PI controller. The active flux error is used to form the compensation of the back EMF through the PI controller, further realize the role of the correction flux.

Next, the transfer function of the CLAFO is derived in detail. From Fig. 9, the expression of the active flux estimated by the CLAFO can be obtained as

$$\begin{cases} \psi_{a\alpha cl} = \int (u_{s\alpha} - R_s i_{s\alpha} - E_{error\,\alpha})\mathrm{d}t - L_q i_{s\alpha} \\ \psi_{a\beta cl} = \int (u_{s\beta} - R_s i_{s\beta} - E_{error\,\beta})\mathrm{d}t - L_q i_{s\beta} \end{cases} \tag{25}$$

where $\psi_{a\alpha cl}$ and $\psi_{a\beta cl}$ are the active flux information obtained by the CLAFO, respectively. $E_{error\alpha}$ and $E_{error\beta}$ are the compensation signals of the back EMF. The compensation signal can be further expressed as

$$\begin{bmatrix} E_{error\alpha} \\ E_{error\beta} \end{bmatrix} = \left(k_p + \frac{k_i}{s}\right) \begin{bmatrix} \psi_{a\alpha cl} - \psi_{a\alpha i} \\ \psi_{a\beta cl} - \psi_{a\beta i} \end{bmatrix} \tag{26}$$

where k_p and k_i are the gains of the PI controller, respectively.

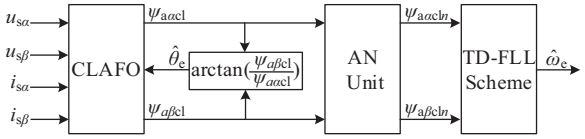

Fig. 10. Block diagram of the proposed speed estimation scheme.

Taking (23) and (26) into (25) can be obtained

$$\psi_{a\alpha\beta cl}(s)=\frac{s^2}{s^2+k_p s+k_i}\psi_{\alpha\beta v}(s)+\frac{k_p s+k_i}{s^2+k_p s+k_i}\psi_{\alpha\beta i}(s) \quad (27)$$

C. Implementations of the Proposed Speed Estimation Scheme

Block diagram of the proposed speed estimation scheme is shown in Fig. 10, the CLAFO with excellent anti-disturbance performance is selected to achieve reliable estimation of active flux (the disturbance rejection of the CLAFO to DC offset and part parameter mismatch is analyzed in the next section). Then, on the basis of obtaining satisfactory active flux, the TD-FLL scheme is applied to estimate the speed accurately.

V. Disturbance Immunity Analysis of the CLAFO

A. Performance Analysis With DC Offset

When DC offset occurs in the system, the VM can be expressed as

$$\begin{bmatrix}\psi_{a\alpha v}^{DC}\\ \psi_{a\beta v}^{DC}\end{bmatrix}=\int\left[\begin{matrix}u_{s\alpha}-R_s i_{s\alpha}+V_\alpha^{DC}(s)\\ u_{s\beta}-R_s i_{s\beta}+V_\beta^{DC}(s)\end{matrix}\right]dt-L_q\begin{bmatrix}i_{s\alpha}\\ i_{s\beta}\end{bmatrix} \quad (28)$$

where $\psi_{a\alpha v}^{DC}$, $\psi_{a\beta v}^{DC}$, V_α^{DC} and V_β^{DC} are α- and β-axis components of the active flux observed by the VM with DC offset, α- and β-axis components of the magnitudes of DC offset, respectively.Thus, putting (28) into (27) yields that

$$\psi_{a\alpha\beta cl}^{DC}(s)=\frac{s^2}{s^2+k_p s+k_i}\psi_{a\alpha\beta v}(s)+\frac{k_p s+k_i}{s^2+k_p s+k_i}\psi_{a\alpha\beta i}(s)+\frac{s\cdot V_{\alpha\beta}^{DC}(s)}{s^2+k_p s+k_i} \quad (29)$$

in which $\psi_{a\alpha\beta cl}^{DC}$ is α- and β-axis components of the active flux observed by the CLAFO with DC offset. The estimated active flux error can be obtained by subtracting (27) from (29), it gives that

$$\Delta\psi_{a\alpha\beta cl}^{DC}(s)=\frac{s}{s^2+k_p s+k_i}V_{\alpha\beta}^{DC}(s) \quad (30)$$

where $\Delta\psi_{a\alpha\beta cl}^{DC}$ is α- and β-axis components of the active flux error with DC offset. The final value theorem can be introduced to analyze the steady-state error of the CLAFO, (30) can be expressed as

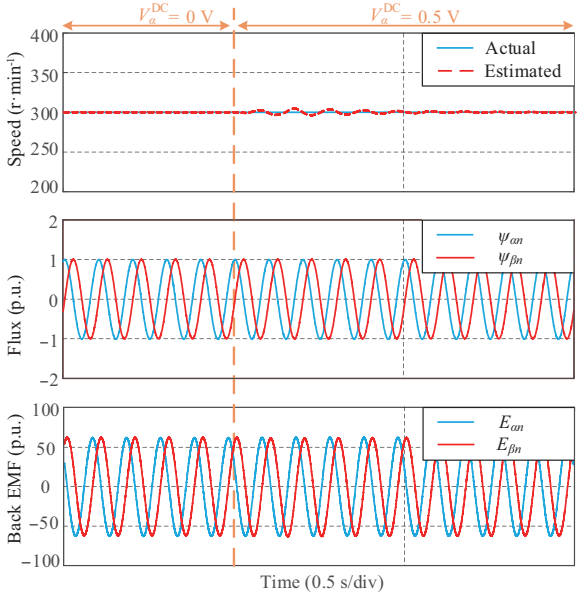

Fig. 11. Estimation performance of the CLAFO with DC offset.

$$\lim_{s\to 0}\Delta\psi_{a\alpha\beta cl}^{DC}(s)=\lim_{s\to 0}s\cdot\frac{s}{s^2+k_p s+k_i}\cdot\frac{V_{\alpha\beta}^{DC}}{s}=0 \quad (31)$$

Seen from (31), the error of the estimated active flux approach 0 with the disturbance of DC offset. That means, the CLAFO can suppress the adverse effects of DC offset, active flux estimated can be guaranteed with absence of the pure integrator.

Compared to the simulation result shown in Fig. 6, the simulation result presented in Fig. 11 demonstrates that the CLAFO can achieve accurate estimation of the active flux even in the presence of DC offset disturbances.

B. Performance Analysis With Stator Resistance Variations

When the stator resistance experience variations, the VM can be expressed as

$$\psi_{a\alpha\beta v}^{R}=\int(u_{s\alpha\beta}-R_s i_{s\alpha\beta}+\Delta R i_{s\alpha\beta})dt-L_q i_{s\alpha\beta} \quad (32)$$

where $\psi_{a\alpha\beta v}^{R}$ and ΔR are α- and β-axis components of the active flux observed by the VM with stator resistance variations and the magnitude of the stator resistance variations, respectively. By substituting (32) into (27), the expression of active flux with stator resistance variations can be obtained as

$$\psi_{a\alpha\beta cl}^{R}(s)=\frac{s^2}{s^2+k_p s+k_i}\psi_{a\alpha\beta v}(s)+\frac{k_p s+k_i}{s^2+k_p s+k_i}\psi_{a\alpha\beta i}(s)+\frac{s\cdot\Delta R i_{s\alpha\beta}(s)}{s^2+k_p s+k_i} \quad (33)$$

where $\psi_{a\alpha\beta cl}^{R}$ is α- and β-axis components of the active flux observed by the CLAFO with stator resistance variations.

Subtracting (27) from (33) yields the active flux estimation error caused by stator resistance variations, it gives that

$$\begin{cases} \Delta\psi^{R}_{\mathrm{a}\alpha\mathrm{cl}}(s) = \dfrac{s}{s^2 + k_{\mathrm{p}}s + k_{\mathrm{i}}}\Delta R I_{\mathrm{s}}\dfrac{s}{s^2 + \omega_{\mathrm{e}}^2} \\ \Delta\psi^{R}_{\mathrm{a}\beta\mathrm{cl}}(s) = \dfrac{s}{s^2 + k_{\mathrm{p}}s + k_{\mathrm{i}}}\Delta R I_{\mathrm{s}}\dfrac{\omega_e}{s^2 + \omega_{\mathrm{e}}^2} \end{cases} \tag{34}$$

in which $\Delta\psi^{R}_{\mathrm{a}\alpha\mathrm{cl}}$, $\psi^{R}_{\mathrm{a}\beta\mathrm{cl}}$ and I_{s} are α- and β-axis components of the active flux error with stator resistance variations and the amplitude of stator current, respectively. To analyze the effect of stator resistance variations on active flux estimation, applying the inverse Laplace transform in (34) can be obtained as [20]

$$\begin{aligned} \Delta\psi^{R}_{\mathrm{a}\alpha\mathrm{cl}} = {} & \Delta R I_{\mathrm{s}}\frac{\omega_{\mathrm{e}}^3\sin(\omega_{\mathrm{e}}t) + k_{\mathrm{p}}\omega_{\mathrm{e}}^2\cos(\omega_{\mathrm{e}}t) - k_{\mathrm{i}}\sin(\omega_{\mathrm{e}}t)}{\omega_{\mathrm{e}}^4 + (k_{\mathrm{p}}^2 - 2k_{\mathrm{i}})\omega_{\mathrm{e}}^2 + k_{\mathrm{i}}^2} + \\ & \Delta R I_{\mathrm{s}}\frac{-k_{\mathrm{p}}\omega_{\mathrm{e}}^2\cosh(a\cdot t)e^{-bt}}{\omega_{\mathrm{e}}^4 + (k_{\mathrm{p}}^2 - 2k_{\mathrm{i}})\omega_{\mathrm{e}}^2 + k_{\mathrm{i}}^2} + \\ & \Delta R I_{\mathrm{s}}\frac{k_{\mathrm{p}}\omega_{\mathrm{e}}^2(\frac{k_{\mathrm{p}}}{2} - \frac{k_{\mathrm{i}}\omega_{\mathrm{e}}^2 - k_{\mathrm{i}}}{k_{\mathrm{p}}\omega_{\mathrm{e}}^2})\sinh(a\cdot t)e^{-bt}}{\left[\omega_{\mathrm{e}}^4 + (k_{\mathrm{p}}^2 - 2k_{\mathrm{i}})\omega_{\mathrm{e}}^2 + k_{\mathrm{i}}^2\right]a} \end{aligned} \tag{35}$$

in which a and b can be expressed as

$$a = \sqrt{\frac{k_{\mathrm{p}}^2}{4} - k_{\mathrm{i}}}\ , \quad b = \frac{k_{\mathrm{p}}}{2} \tag{36}$$

When the motor is running in the high-speed range, the approximate expression can be obtained as

$$\omega_{\mathrm{e}} \gg \sin(\omega_{\mathrm{e}}t)\ ,\ \omega_{\mathrm{e}} \gg \cos(\omega_{\mathrm{e}}t) \tag{37}$$

Subsequently,

$$\lim_{t\to\infty}\Delta R I_{\mathrm{s}}\frac{\omega_{\mathrm{e}}^3\sin(\omega_{\mathrm{e}}t) + k_{\mathrm{p}}\omega_{\mathrm{e}}^2\cos(\omega_{\mathrm{e}}t) - k_{\mathrm{i}}\sin(\omega_{\mathrm{e}}t)}{\omega_{\mathrm{e}}^4 + (k_{\mathrm{p}}^2 - 2k_{\mathrm{i}})\omega_{\mathrm{e}}^2 + k_{\mathrm{i}}^2} \approx 0 \tag{38}$$

$$\lim_{t\to\infty}\Delta R I_{\mathrm{s}}\frac{-k_{\mathrm{p}}\omega_{\mathrm{e}}^2\cosh(a\cdot t)e^{-bt}}{\omega_{\mathrm{e}}^4 + (k_{\mathrm{p}}^2 - 2k_{\mathrm{i}})\omega_{\mathrm{e}}^2 + k_{\mathrm{i}}^2} = 0 \tag{39}$$

$$\lim_{t\to\infty}\Delta R I_{\mathrm{s}}\frac{k_{\mathrm{p}}\omega_{\mathrm{e}}^2(\frac{k_{\mathrm{p}}}{2} - \frac{k_{\mathrm{i}}\omega_{\mathrm{e}}^2 - k_{\mathrm{i}}}{k_{\mathrm{p}}\omega_{\mathrm{e}}^2})\sinh(a\cdot t)e^{-bt}}{\left[\omega_{\mathrm{e}}^4 + (k_{\mathrm{p}}^2 - 2k_{\mathrm{i}})\omega_{\mathrm{e}}^2 + k_{\mathrm{i}}^2\right]a} = 0 \tag{40}$$

With (38), (39) and (40), the time domain analysis is carried out to show that the estimated active flux error caused by the variations of stator resistance can also approach 0 when the motor runs at the medium-speed or high-speed range. Therefore, the CLAFO can deal with the issues of stator resistance variations, promises a satisfactory active flux estimation.

C. Performance Analysis With d-Axis Inductance Variations

The effects of the *d*-axis inductance variations on the active flux estimation are further discussed. Seen from Fig. 9, the *d*-axis inductance parameter only exists in the CM, and the α-axis active flux expression with the *d*-axis inductance variations can be obtained

$$\begin{aligned} \psi^{LD}_{\mathrm{a}\alpha\mathrm{cl}}(s) = {} & \frac{s^2}{s^2 + k_{\mathrm{p}}s + k_{\mathrm{i}}}\psi_{\mathrm{a}\alpha\mathrm{v}}(s) + \frac{k_{\mathrm{p}}s + k_{\mathrm{i}}}{s^2 + k_{\mathrm{p}}s + k_{\mathrm{i}}}\psi_{\mathrm{a}\alpha i}(s) + \\ & \frac{k_{\mathrm{p}}s + k_{\mathrm{i}}}{s^2 + k_{\mathrm{p}}s + k_{\mathrm{i}}}i_d\Delta L_d\cos\hat{\theta}(s) \end{aligned} \tag{41}$$

where ΔL_d and $\psi^{LD}_{\mathrm{a}\alpha\mathrm{cl}}$ are the magnitude of the *d*-axis inductance variations, α-axis components of the active flux observed by the CLAFO with *d*-axis inductance variations, respectively. By subtracting (27) from (41), the estimated active flux error with the *d*-axis inductance variations can be obtained

$$\Delta\psi^{LD}_{\mathrm{a}\alpha\mathrm{cl}}(s) = \frac{k_{\mathrm{p}}s + k_{\mathrm{i}}}{s^2 + k_{\mathrm{p}}s + k_{\mathrm{i}}}\Delta L_d I_d\frac{s}{s^2 + \omega_{\mathrm{e}}^2} \tag{42}$$

in which $\Delta\psi^{LD}_{\mathrm{a}\alpha\mathrm{cl}}$ is α-axis components of the estimated active fluxerror with *d*-axis inductance variations. Similarly, applying the inverse Laplace transform in (42) can be obtained

$$\begin{aligned} \Delta\psi^{LD}_{\mathrm{a}\alpha\mathrm{cl}} = {} & \Delta L_d I_{\mathrm{s}}\frac{(k_{\mathrm{i}} - \omega_{\mathrm{e}}^2 k_{\mathrm{i}} + \omega_{\mathrm{e}}^2 k_{\mathrm{p}}^2)\cos(\omega_{\mathrm{e}}t) + \omega_{\mathrm{e}}^3 k_{\mathrm{p}}\sin(\omega_{\mathrm{e}}t)}{\omega_{\mathrm{e}}^4 + (k_{\mathrm{p}}^2 - 2k_{\mathrm{i}})\omega_{\mathrm{e}}^2 + k_{\mathrm{i}}^2} + \\ & \Delta L_d I_{\mathrm{s}}[-\frac{(-k_{\mathrm{i}}\omega_{\mathrm{e}}^2 + k_{\mathrm{p}}^2\omega_{\mathrm{e}}^2 + k_{\mathrm{i}}^2)}{\omega_{\mathrm{e}}^4 + (k_{\mathrm{p}}^2 - 2k_{\mathrm{i}})\omega_{\mathrm{e}}^2 + k_{\mathrm{i}}^2}\cosh(a\cdot t)e^{-bt}] + \\ & \Delta L_d I_{\mathrm{s}}\left\{\begin{array}{l} \dfrac{(-k_{\mathrm{i}}\omega_{\mathrm{e}}^2 + k_{\mathrm{p}}^2\omega_{\mathrm{e}}^2 + k_{\mathrm{i}}^2)}{[\omega_{\mathrm{e}}^4 + (k_{\mathrm{p}}^2 - 2k_{\mathrm{i}})\omega_{\mathrm{e}}^2 + k_{\mathrm{i}}^2]a} \\ \times(\dfrac{k_{\mathrm{p}}}{2} - \dfrac{k_{\mathrm{i}}k_{\mathrm{p}}\omega_{\mathrm{e}}^2}{-k_{\mathrm{i}}\omega_{\mathrm{e}}^2 + k_{\mathrm{p}}^2\omega_{\mathrm{e}}^2 + k_{\mathrm{i}}^2}) \end{array}\right\}\sinh(a\cdot t)e^{-bt} \end{aligned} \tag{43}$$

Referring to (35)–(40), (43) can be finally expressed as

$$\lim_{t\to\infty}\Delta\psi^{LD}_{\mathrm{a}\alpha\mathrm{cl}} \approx 0 \tag{44}$$

With (44), it is indicated that when the *d*-axis inductance variations occur in the CLAFO, the active flux error will approach 0 with time. It is concluded from above analysis that the CLAFO can ensure a reliable estimation of active flux.

VI. Experimental Results

To verify the performance of the proposed TD-FLL scheme for IPMSM drives, extensive experimental tests are performed based on the block diagram of the overall sensorless control of IPMSM drives (see Fig. 12). The test bench of IPMSM drives is shown in Fig. 13, which includes a 3-kW IPMSM, an induction motor (emulated as the load), two inverters, an oscilloscope, and a host computer. The parameters of the test bench are listed in Table I.

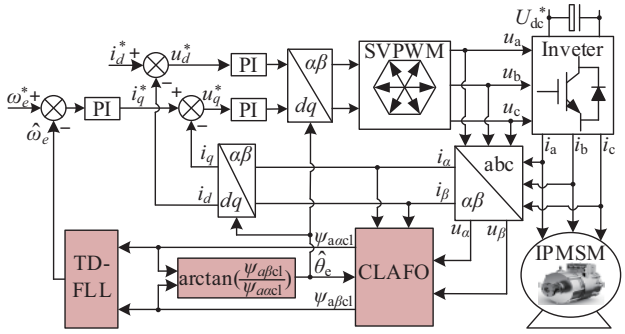

Fig. 12. Block diagram of sensorless control system for IPMSM.

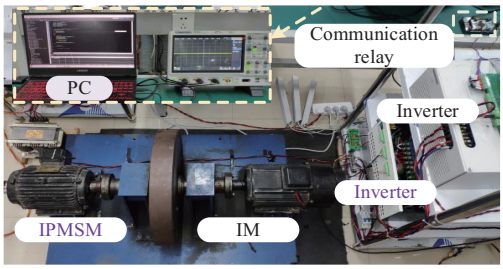

Fig. 13. Experimental set-up of a 3-kW IPMSM.

TABLE I
PARAMETERS OF THE IPMSM DRIVES SYSTEM

Parameter	Value	Parameter	Value
Rated power	3 kW	DC bus voltage	600 V
Rated voltage	380 V	Stator resistance	2.1 Ω
Rated current	6.5 A	*d*-axis inductance	70 mH
Rated speed	1500 r/min	*q*-axis inductance	270 mH
Pole pairs	2	Permanent magnetic flux	0.725 Wb

Focusing on the position estimation of the QPLL under ADCs, the speed command is set to 100 r/min → 500 r/min →100 r/min, the experimental test result is shown in Fig. 14. As seen from Fig. 14, the position estimation error under ADCs exceeds 0.25 rad, which will impact the stable operation of the sensorless control system for IPMSM.

To verify the speed estimation performance of the TD-FLL scheme under ADCs and compared to that of the SOGI-FLL scheme. The speed command is set to 100 r/min → 500 r/min→ 100 r/min, the experimental result in Fig. 15 shows the estimated speed of the TD-FLL scheme is almost identical to the actual speed, the estimated error is within a reasonable range. For comparison, set the same experimental conditions, Fig. 16 presents a speed estimation performance of the SOGI-FLL scheme under ADCs. To make a clear illustration, the performance comparison of the two schemes is concluded in Tables II and III. As indicated in Tables II and III, the TD-FLL scheme exhibits superior performance in terms of speed estimation accuracy under ADCs.

The sensorless control technology for IPMSM drives is expected to possess good estimation performance with load of sudden increasing and decreasing. As shown in Figs. 17 and

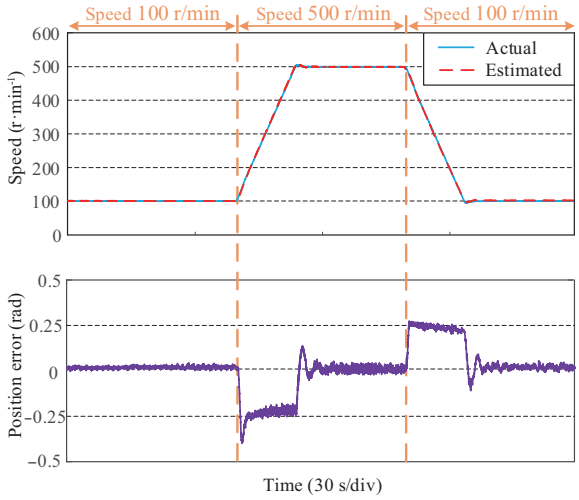

Fig. 14. Speed estimation performance of the QPLL under ADCs.

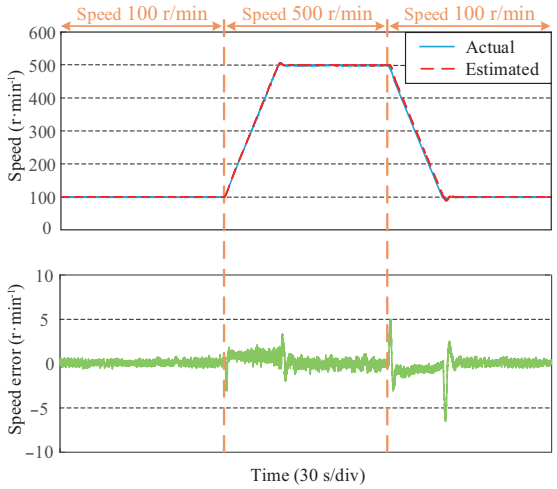

Fig. 15. Speed estimation performance of the TD-FLL under ADCs.

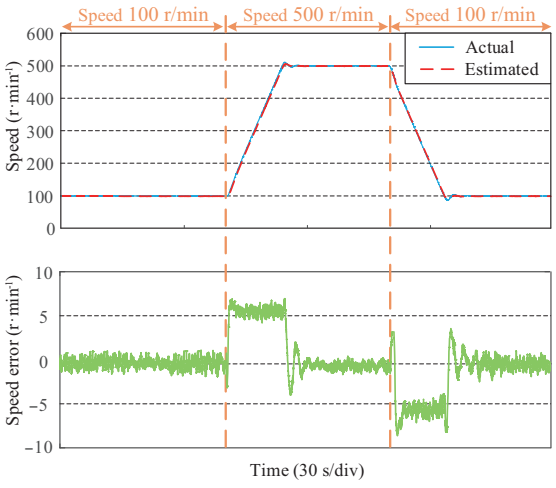

Fig. 16. Speed estimation performance of the SOGI-FLL under ADCs.

18, the speed command is set to 300 r/min and the load is set to 0 N·m → 8 N·m → 0 N·m, respectively. The results in Figs.

TABLE II
PERFORMANCE COMPARISON BETWEEN THE TD-FLL SCHEME AND THE SOGIFLL SCHEME UNDER ACCELERATION CASES r/min

Scheme	MAX	MIN	MSE	RMS
TD-FLL	3.100	−3.300	0.6209	0.7063
SOGI-FLL	6.900	− 4.200	− 4.4036	4.6391

TABLE III
PERFORMANCE COMPARISON BETWEEN THE TD-FLL SCHEME AND THE SOGIFLL SCHEME UNDER DECELERATION CASES r/min

Scheme	MAX	MIN	MSE	RMS
TD-FLL	4.800	−6.700	−0.765	0.825
SOGI-FLL	4.200	−9.600	−4.670	4.690

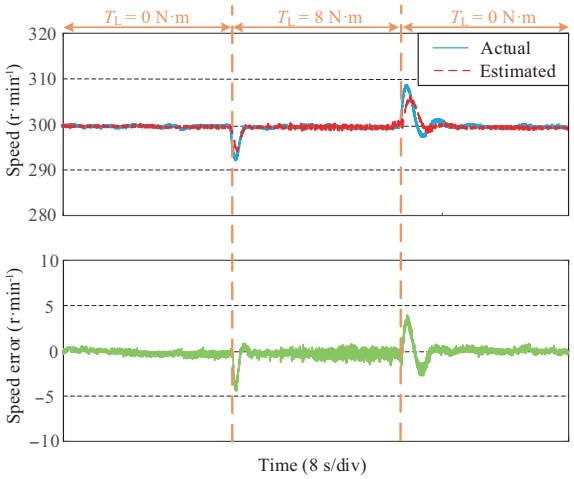

Fig. 17. Speed estimation performance of the TD-FLL with load of sudden increasing and decreasing.

17 and 18 indicate that the TD-FLL scheme and conventional SOGI-FLL scheme can respond quickly and possess acceptable dynamic estimation performance.

Fig. 19 presents the suppression performance of the CLAFO with DC offset disturbance. The speed command is set to 300 r/min and the magnitude of DC offset is set to 0 V → 5 V → 0 V → –5 V, respectively. As shown in Fig. 19, when DC offset occurs in the CLAFO, the estimated speed and position information undergo a brief, slight oscillation followed by rapid convergence. The performance of the CLAFO with DC offset under low-speed range is further explored. Seen from Fig. 20, the speed command is set to 100 r/min and maintaining the same DC offset settings. Fig. 20 shows that the CLAFO can deal with DC offset disturbance under low-speed range and achieve good estimation performance.

Finally, the inhibitive effects of the CLAFO on the disturbance of stator resistance variations and *d*-axis inductance variations are focused on. The experimental results with stator resistance variations as shown in Fig. 21, in which the speed command is set to 300 r/min and the magnitude of the stator resistance variations are set to 0 Ω→ 1.4 Ω → 0 Ω → –1.4 Ω, respectively. Seen from Fig. 22, suppression performance of

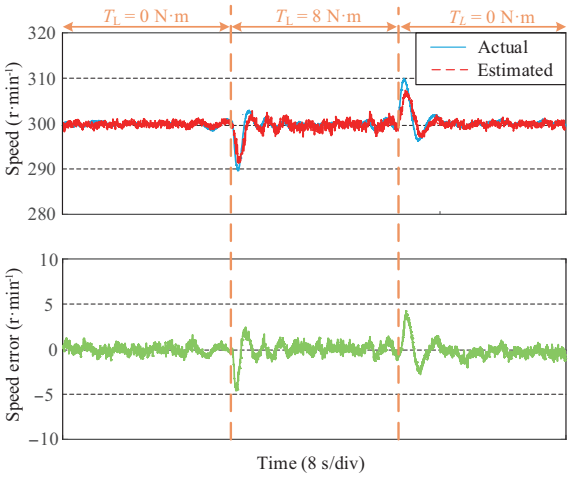

Fig. 18. Speed estimation performance of the SOGI-FLL with load of sudden increasing and decreasing.

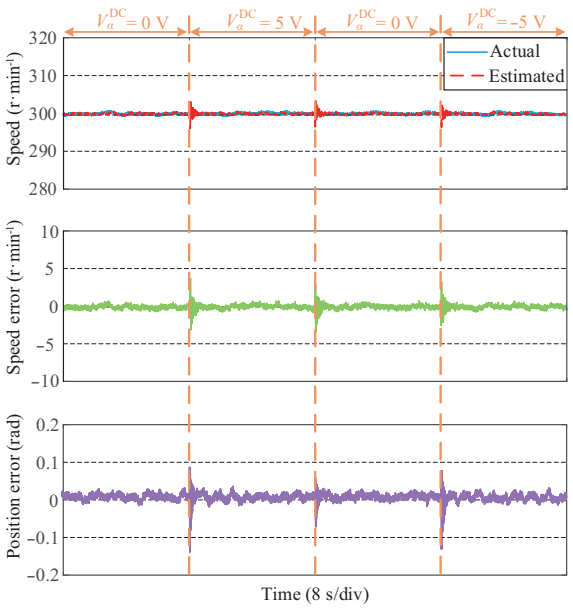

Fig. 19. Suppression performance of the CLAFO with DC offset.

the CLAFO with *d*-axis inductance variations is presented. The speed command is set to 300 r/min and the magnitude of the *d*-axis inductance variations are set to 0 mH→70 mH → 0 mH →–70 mH, respectively. It can be seen from Figs. 21 and 22 that by introducing CLAFO, the estimated speed convergent rapidly and the estimated position has negligible deviation when stator resistance variations or *d*-axis inductance variations occur in IPMSM drives.

To sum up, the proposed speed estimation scheme improves the estimation accuracy under ADCs while ensuring a good stability margin and dynamic performance of the system. The CLAFO achieves satisfactory suppression of DC offset, stator resistance variations and *d*-axis inductance variations disturbance, and improve the robustness of the sensorless control system for IPMSM.

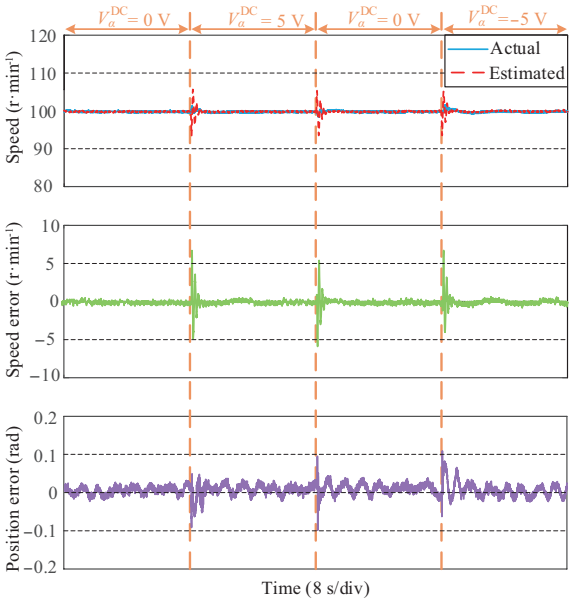

Fig. 20. Suppression performance of the CLAFO with DC offset under lowspeed range.

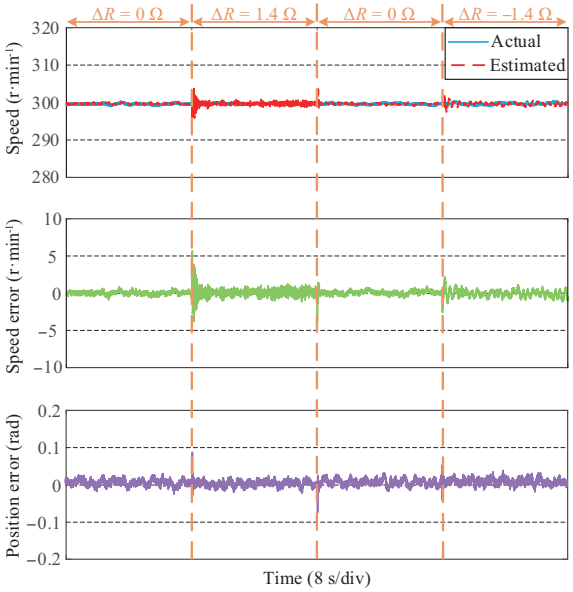

Fig. 21. Suppression performance of the CLAFO with stator resistance variations.

VII. Conclusion

The applicability of the QPLL scheme and the SOGI-FLL under ADCs may be challenged. To address this, an estimation scheme based on the CLAFO and the TD-FLL was proposed in this paper for IPMSM drives. In the proposed estimation scheme, the TD-FLL was carefully designed to improve estimation accuracy and the CLAFO was used to enhance the disturbance mitigation capability of the proposed estimation scheme. The performance of the proposed estimation scheme under different cases was extensively investigated through experimental tests. The results point out that the proposed estimation scheme achieves two interesting benefits of accurate estimation under ADCs and good disturbance rejection.

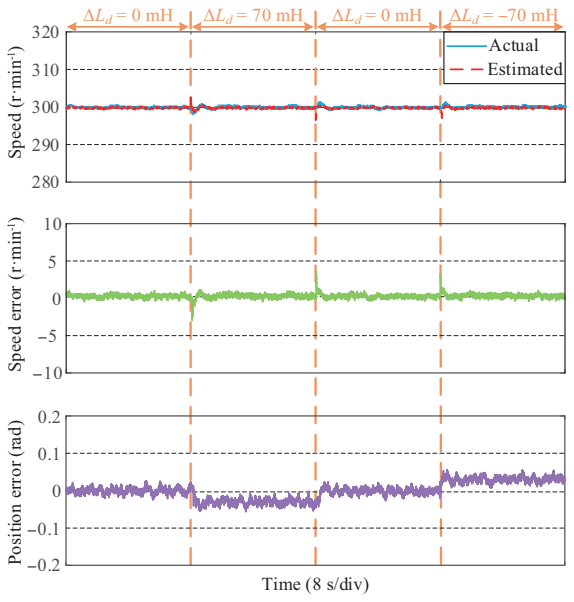

Fig. 22. Suppression performance of the CLAFO with *d*-axis inductance variations.

References

[1] G. Wang, M. Valla, and J. Solsona, "Position sensorless permanent magnet synchronous machine drives—A review," in *IEEE Transactions on Industrial Electronics*, vol. 67, no. 7, pp. 5830–5842, Jul. 2020.

[2] Y. Zuo, H. Wang, X. Ge, Y. Liu, S. Zhu, and C. H. T. Lee, "A simple current measurement scaling error compensation method for PMSM drives," in *IEEE Transactions on Power Electronics*, vol. 39, no. 11, pp. 14122–14128, Nov. 2024.

[3] O. C. Kivanc and S. B. Ozturk, "Sensorless PMSM drive based on stator feedforward voltage estimation improved with MRAS multiparameter estimation," in *IEEE/ASME Transactions on Mechatronics*, vol. 23, no. 3, pp. 1326–1337, Jun. 2018.

[4] H. Yan, W. Wang, Y. Xu, and J. Zou, "Position sensorless control for PMSM drives with single current sensor," in *IEEE Transactions on Industrial Electronics*, vol. 70, no. 1, pp. 178–188, Jan. 2023.

[5] F. Betin, G. A. Capolino, D. Casadei, B. Kawkabani, R. I. Bojoi, L. Harnefors, E. Levi, L. Parsa, and B. Fahimi, "Trends in electrical machines control: Samples for classical, sensorless, and fault-tolerant techniques," in *IEEE Industrial Electronics Magazine*, vol. 8, no. 2, pp. 43–55, Jun. 2014.

[6] C. Gong, Y. Hu, J. Gao, Y. Wang, and L. Yan, "An improved delay suppressed sliding-mode observer for sensorless vector-controlled PMSM," in *IEEE Transactions on Industrial Electronics*, vol. 67, no. 7, pp. 5913–5923, Jul. 2020.

[7] Y. Zuo, H. Wang, X. Ge, J. Mu, C. Lin, and C. H. T. Lee, "A novel single phase current sensor control strategy based on dual APF-QSG for position sensorless IPMSM drives," in *IEEE Transactions on Power Electronics*, vol. 39, no. 1, pp. 71–77, Jan. 2024.

[8] S. Ye and X. Yao, "An enhanced SMO-based permanent-magnet synchronous machine sensorless drive scheme with current measurement error compensation," in *IEEE Journal of Emerging and Selected Topics in Power Electronics*, vol. 9, no. 4, pp. 4407–4419, Aug. 2021.

[9] I. Boldea, M. C, Paicu, and G. Andreescu, "Active flux concept for motion sensorless unified AC drives," in *IEEE Transactions on Power Electronics*, vol. 23, no. 5, pp. 2612–2618, Sept. 2008.

[10] I. Boldea, A. -A. Popa, and F. Blaabjerg, "Active flux based advanced

encoderless AC drives: A tutorial review," in *IEEE Transactions on Power Electronics*, vol. 39, no. 10, pp. 13510–13523, Oct. 2024.
[11] A. T. Nguyen, M. S. Rafaq, H. H. Choi, and J.-W. Jung, "A model reference adaptive control based speed controller for a surface-mounted permanent magnet synchronous motor drive," in *IEEE Transactions on Industrial Electronics*, vol. 65, no. 12, pp. 9399–9409, Dec. 2018.
[12] X. Sun, Y. Zhang, X. Tian, J. Cao, and J. Zhu, "Speed sensorless control for IPMSMs using a modified MRAS with gray wolf optimization algorithm," in *IEEE Transactions on Transportation Electrification*, vol. 8, no. 1, pp. 1326–1337, Mar. 2022.
[13] N. K. Quang, N. T. Hieu, and Q. P. Ha, "FPGA-based sensorless PMSM speed control using reduced-order extended Kalman filters," in *IEEE Transactions on Industrial Electronics*, vol. 61, no. 12, pp. 6574–6582, Dec. 2014.
[14] A. Apte, V. A. Joshi, H. Mehta, and R. Walambe, "Disturbance-observer based sensorless control of PMSM using integral state feedback controller," in *IEEE Transactions on Power Electronics*, vol. 35, no. 6, pp. 6082–6090, Jun. 2020.
[15] H. X. Nguyen, T. N. C. Tran, J. W. Park, and J. W. Jeon, "An adaptive linear neuron based third-order PLL to improve the accuracy of absolute magnetic encoders," in *IEEE Transactions on Industrial Electronics*, vol. 66, no. 6, pp. 4639–4649, Jun. 2019.
[16] Y. Zhang, Z. Yin, C. Bai, G. Wang, and J. Liu, "A rotor position and speed estimation method using an improved linear extended state observer for IPMSM sensorless drives," in *IEEE Transactions on Power Electronics*, vol. 36, no. 12, pp. 14062–14073, Dec. 2021.
[17] H. Wang, X. Ge, Y. Yue, and Y. C. Liu, "Dual phase-locked loop-based speed estimation scheme for sensorless vector control of linear induction motor drives," in *IEEE Transactions on Industrial Electronics*, vol. 67, no. 7, pp. 5900–5912, Jul. 2020.
[18] H. A. Hamed and M. S. El Moursi, "A new type-2 PLL based on unit delay phase angle error compensation during the frequency ramp," in *IEEE Transactions on Power Systems*, vol. 34, no. 4, pp. 3289–3293, Jul. 2019.
[19] H. Wang, Y. Yang, X. Ge, Y. Zuo, Y. Yue, and S. Li, "PLL- and FLL based speed estimation schemes for speed-sensorless control of induction motor drives: review and new attempts," in *IEEE Transactions on Power Electronics*, vol. 37, no. 3, pp. 3334–3356, Mar. 2022.
[20] H. Wang, Y. Yang, X. Ge, Y. Zuo, X. Feng, D. Chen, and Y. C. Chen, "Speed-sensorless control of induction motor drives with a STA-FLL speed estimation scheme," in *IEEE Transactions on Industrial Electronics*, vol. 70, no. 12, pp. 12168–12180, Dec. 2023.
[21] H. A. Beshr, M. S. E. Moursi, H. A. Hamed, and A. Al-Sumaiti, "Advanced type-1c FLL for enhancing converters synchronization during frequency drift," in *IEEE Transactions on Power Delivery*, vol. 36, no. 2, pp. 1063–1078, Apr. 2021.
[22] H. X. Nguyen, T. N. Tran, J. W. Park, N. V. P. Tran, and J. W. Jeon, "Improving the accuracy of battery-free multiturn absolute magnetic encoders by using a self-referencing lookup table algorithm," in *IEEE Transactions on Instrumentation and Measurement*, vol. 69, no. 8, pp. 5468–5477, Aug. 2020.
[23] J. Han, "From PID to active disturbance rejection control," in *IEEE Transactions on Industrial Electronics*, vol. 56, no. 3, pp. 900–906, Mar. 2009.

Sibo Wan received the B.Eng. degree in electrical engineering and automation from East China Jiaotong University, Nanchang, China, in 2023. He is currently working toward the M.Eng. degree in electrical engineering with Southwest Jiaotong University, Chengdu, China. His current research is sensorless control of permanent magnet synchronous motor drive systems.

Huimin Wang received the B.Eng. and Ph.D. degrees from Southwest Jiaotong University (SWJTU), Chengdu, China, in 2016 and 2021, respectively, both in electrical engineering.

From October 2019 to October 2020, he has been a Visiting Ph.D. Student with the Department of Energy Technology, Aalborg University, Denmark. He is currently an Assistant Professor with SWJTU. His research interests include ac motor drive system and its speed-sensorless control, synchronization techniques in grid-connected system, and reliability evaluation in traction drives.

Dr. Wang was a recipient of one ESI Highly Cited Paper on *IEEE Journal of Emerging and Selected Topics in Power Electronics*, and a recipient of the Best Paper Award of IEEE Transportation Electrification Conference and EXPO Asia-Pacific (ITEC Asia-Pacific) in 2019.

Yun Zuo received the B.Eng. degree in electrical engineering and automation from Dalian Jiaotong University, Dalian, China, in 2019. He is currently working toward the Ph.D. degree in electrical engineering with Southwest Jiaotong University, Chengdu, China. His research interests include ac motor drive systems and its sensor fault tolerance and sensorless control.

Gaoli Guo received the B.Eng. degree in automation from Henan University of Technology, Zhengzhou, China, in 2022. He is currently working toward the M.Eng. degree in electrical engineering with Southwest Jiaotong University, Chengdu, China. His research interests are condition monitoring and fault diagnosis of permanent magnet synchronous motors.

Xinglai Ge received the B.S., M.S., and Ph.D. degrees in electrical engineering from Southwest Jiaotong University (SWJTU), Chengdu, China, in 2001, 2004, and 2010, respectively. He is currently a Full Professor with the School of Electrical Engineering, Southwest Jiaotong University and a Vice Director of Department of Power Electronics and Power Drive. From October 2013 to October 2014, he was a visiting scholar at the School of Electrical and Computer Engineering, Georgia Institute of Technology, Atlanta, GA, USA. He is the author and co-author of more than 70 technical papers. His research interests include stability analysis and control of electrical traction system, fault diagnosis and reliability evaluation of traction converter and motor drive system.